

Tunable symmetry breaking and helical edge transport in a graphene quantum spin Hall state

A. F. Young^{1*}, J. D. Sanchez-Yamagishi^{1*}, B. Hunt^{1*}, S. H. Choi¹, K. Watanabe², T. Taniguchi², R. C. Ashoori¹ & P. Jarillo-Herrero¹

Low-dimensional electronic systems have traditionally been obtained by electrostatically confining electrons, either in heterostructures or in intrinsically nanoscale materials such as single molecules, nanowires and graphene. Recently, a new method has emerged with the recognition that symmetry-protected topological (SPT) phases^{1,2}, which occur in systems with an energy gap to quasiparticle excitations (such as insulators or superconductors), can host robust surface states that remain gapless as long as the relevant global symmetry remains unbroken. The nature of the charge carriers in SPT surface states is intimately tied to the symmetry of the bulk, resulting in one- and two-dimensional electronic systems with novel properties. For example, time reversal symmetry endows the massless charge carriers on the surface of a three-dimensional topological insulator with helicity, fixing the orientation of their spin relative to their momentum^{3,4}. Weakly breaking this symmetry generates a gap on the surface⁵, resulting in charge carriers with finite effective mass and exotic spin textures⁶. Analogous manipulations have yet to be demonstrated in two-dimensional topological insulators, where the primary example of a SPT phase is the quantum spin Hall state^{7,8}. Here we demonstrate experimentally that charge-neutral monolayer graphene has a quantum spin Hall state^{9,10} when it is subjected to a very large magnetic field angled with respect to the graphene plane. In contrast to time-reversal-symmetric systems⁷, this state is protected by a symmetry of planar spin rotations that emerges as electron spins in a half-filled Landau level are polarized by the large magnetic field. The properties of the resulting helical edge states can be modulated by balancing the applied field against an intrinsic antiferromagnetic instability^{11–13}, which tends to spontaneously break the spin-rotation symmetry. In the resulting canted antiferromagnetic state, we observe transport signatures of gapped edge states, which constitute a new kind of one-dimensional electronic system with a tunable bandgap and an associated spin texture¹⁴.

In the integer quantum Hall effect, the topology of the bulk Landau-level energy bands requires the existence of gapless edge states at any interface with the vacuum. The metrological precision of the Hall quantization can be traced to the inability of these edge states to back-scatter due to the physical separation of modes with opposite momenta by the insulating sample bulk. In contrast, counterpropagating boundary states in a SPT insulator coexist spatially but are prevented from backscattering by a symmetry of the experimental system^{3,4}. The local symmetry that protects transport in SPT surface states is unlikely to be as robust as the inherently nonlocal physical separation that protects the quantum Hall effect. However, it enables the creation of new electronic systems in which momentum and some quantum number such as spin are coupled, potentially leading to devices with new functionality. Most experimentally realized SPT phases are based on time reversal symmetry (TRS), with counterpropagating states protected from intermixing by the Kramers degeneracy. However, intensive efforts are under way to search for topological phases protected by symmetries other than time reversal in new experimental systems^{15,16}.

Our approach is inspired by the similarity between the TRS quantum spin Hall (QSH) state and overlapping electron- and hole-like copies of the quantum Hall effect, with the two copies having opposite spin polarizations. This state is protected by spin conservation rather than the orthogonality of states in a Kramers doublet³, as with the TRS QSH observed in systems with strong spin-orbit coupling. Nevertheless, it is expected to reproduce the characteristic experimental signatures of the TRS QSH, with gapless helical edge states enclosing an insulating bulk^{9,10}. Two requirements are necessary for such a QSH state. First, the spin-orbit coupling must be weak, so that spin remains a good quantum number. Second, the energy gap between electron- and hole-like Landau levels must be small enough to be invertible by the Zeeman splitting. Both of these conditions are met in graphene, which is a gapless semimetal with very weak spin-orbit coupling¹⁷. The graphene Landau-level structure is characterized by the existence of a fourfold spin- and valley-degenerate Landau level at zero energy¹⁸ (zLL). Near the sample boundary, the zLL splits into one positively dispersing (electron-like) and one negatively dispersing (hole-like) mode per spin projection. Consequently, a spin-symmetry-protected QSH state is expected when the spin degeneracy is lifted by an external magnetic field, resulting in a bulk energy gap at charge neutrality and electron- and hole-like states with opposite spin polarizations that cross at the sample edge^{9,10}.

Experimentally, charge-neutral monolayer graphene does not exhibit the expected phenomenology of the QSH state, becoming strongly insulating instead at high magnetic fields¹⁹. Although the precise nature of this insulating state has remained elusive, its origin can be traced to the strong Coulomb interactions within the graphene zLL. At integer filling factors, v , the Coulomb energy is minimized by forming antisymmetric orbital wavefunctions, forcing the combined spin-valley isospin part of the wavefunction to be symmetric. The resulting possible ground states lie on a degenerate manifold of states fully polarized in the approximately SU(4)-symmetric isospin space²⁰, encompassing a variety of different spin and valley orders. In the real experimental system, the state at any given filling factor (such as $v = 0$) is determined by the competition between SU(4) symmetry-breaking effects. The most obvious such anisotropy is the Zeeman effect, which naturally favours a spin-polarized state, but the sublattice structure of the zLL adds additional interaction anisotropies²¹ that can favour spin-unpolarized ground states characterized by lattice-scale spin- or charge-density-wave order^{11–13,22}. This interplay can be probed experimentally by changing the in-plane component of the magnetic field, which changes the Zeeman energy but does not affect orbital energies, and previous observations indeed confirm that the state responsible for the $v = 0$ insulator is spin unpolarized²³. However, the spin-polarized QSH state can be expected to emerge for a sufficiently large in-plane field, manifesting as an incompressible conducting state at charge neutrality.

Figure 1a shows two-terminal conductance measurements of a high-quality graphene device fabricated on a thin hexagonal boron nitride substrate, which itself sits on a graphite local gate. As the total magnetic field (B_T) is increased with B_{\perp} , the component perpendicular to the

¹Department of Physics, Massachusetts Institute of Technology, Cambridge, Massachusetts 02139, USA. ²Advanced Materials Laboratory, National Institute for Materials Science, 1-1 Namiki, Tsukuba 305-0044, Japan.

*These authors contributed equally to this work.

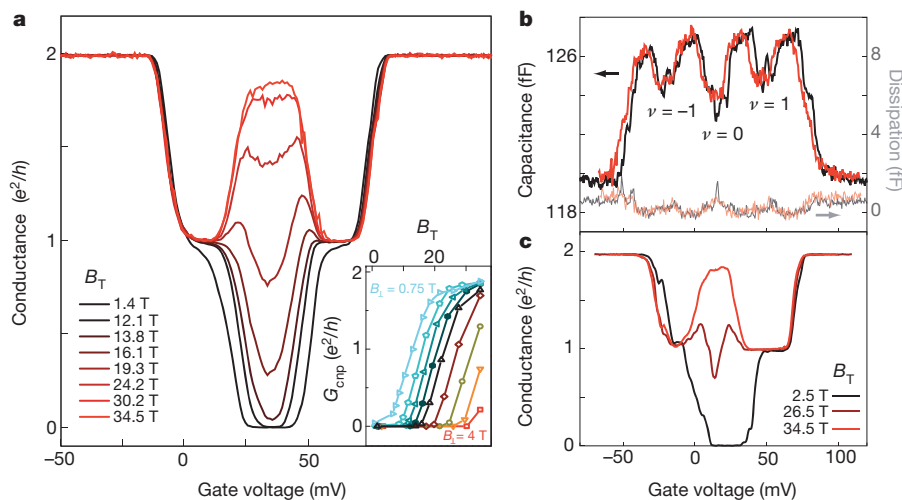


Figure 1 | QSH state in monolayer graphene in extreme tilted magnetic fields. **a**, Conductance of device A at $B_{\perp} = 1.4$ T for different values of B_T . As B_T increases, the insulating state at $\nu = 0$ is gradually replaced by a high-conductance state, with an accompanying inversion of the sign of $\partial G_{\text{cnp}} / \partial T$ (additional data in Extended Data Figs 2 and 3). Inset, G_{cnp} as a function of B_T for device A: $B_{\perp} = 0.75, 1.0, 1.4, 1.6, 2.0, 2.5, 3.0$ and 4.0 T (left to right). **b**, Capacitance (opaque lines) and dissipation (semi-opaque lines) of device B at

$B_{\perp} = 2.5$ T. The low dissipation confirms that the measurements are in the low-frequency limit, such that the dips in capacitance can be interpreted as corresponding to incompressible states. **c**, Conductance under the same conditions. The absence of a detectable change in capacitance, even as the two-terminal conductance undergoes a transition from an insulating state to a metallic state (Extended Data Fig. 6), suggests that the conductance transition is due to the emergence of gapless edge states.

device plane, held constant, the initially low charge-neutrality point conductance (G_{cnp}) increases steadily before finally saturating at $G \approx 1.8e^2/h$ for the largest total field applied (e , electron charge; h , Planck's constant). Evidence for a similar transition was recently reported in bilayer graphene²⁴, where the additional orbital degeneracy

of the zLL leads to a conductance of $4e^2/h$. We note that although superficially similar, the structure and transport properties of the resulting edge modes are likely to be heavily influenced by the additional degeneracy, particularly when many-body reconstructions of the edge states are taken into account^{10,25}.

To distinguish the roles of the edges and the bulk in this conductance transition, we also measure the capacitance between the graphene and the graphite back gate under similar conditions. Capacitance (C) measurements serve as a probe of the bulk density of states (D) via $C^{-1} = C_G^{-1} + (Ae^2D)^{-1}$, where C_G is the geometric capacitance and A is the sample area. Simultaneous capacitance and transport measurements from a second graphene device show that quantized Hall states within the zLL at $\nu = 0$ and $\nu = \pm 1$ are associated with minima in the density of states (Fig. 1b, c). As the total field is increased, the capacitance dip at $\nu = 0$ remains unaltered even as the conductance increases

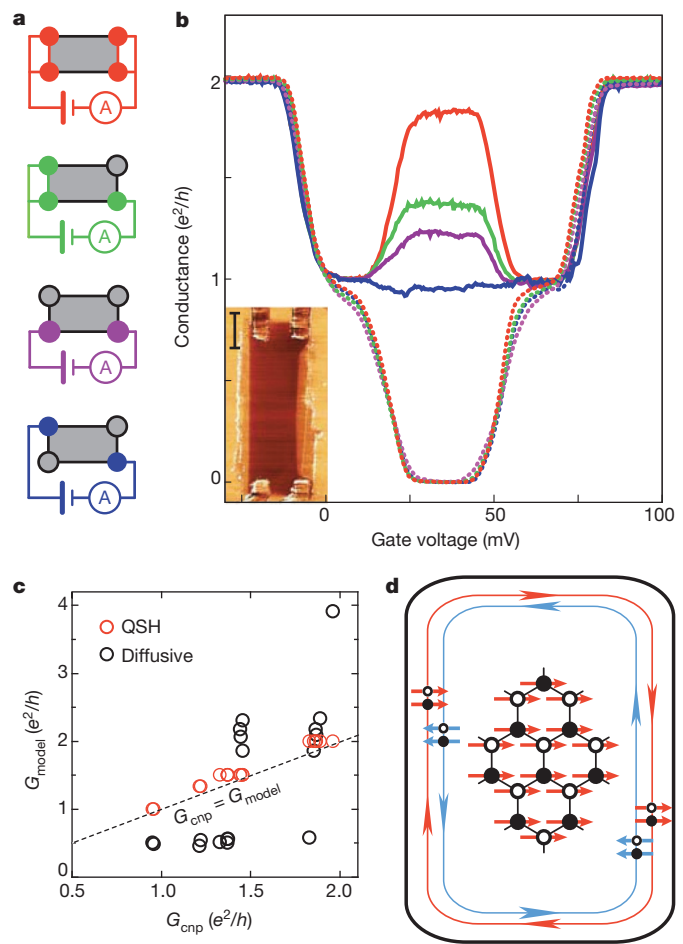


Figure 2 | Nonlocal two-terminal transport in the QSH regime. **a**, Schematic diagram of four distinct two-terminal measurement topologies available in a four-terminal device. Open circles indicate floating contacts whereas filled, coloured circles indicate measurement contacts. Each variation probes two parallel conductance paths between the measurement contacts with a variable number of segments on each path, indicated by black edges. **b**, Two-terminal conductance measurements of device A for $B_{\perp} = 1.4$ T, colour-coded to match the four different measurement configurations. Dashed curves correspond to $B_T = 1.4$ T; solid curves correspond to $B_T = 34.5$ T (QSH regime). In the QSH regime, G_{cnp} depends strongly on the number of floating contacts (see Extended Data Fig. 4 for similar data for device C). Inset, atomic force microscope (AFM) phase micrograph of device A; scale bar, $1 \mu\text{m}$. **c**, G_{cnp} for eighteen different contact configurations based on cyclic permutations of the topologies shown in a. Data are plotted against two model fits. In a numerical simulation based on a diffusive model (black circles), the graphene flake was assumed to be a bulk conductor with the conductivity left as a fitting parameter ($\sigma = 3.25e^2/h$ for the best fit). The QSH model (red circles) is equation (1) and has no fitting parameters. The dashed line indicates a perfect fit of data to model. We note that the measured G_{cnp} never reaches the value predicted by the QSH model, indicating either contact resistance or finite backscattering between the helical edge states. **d**, Schematic diagram of bulk order and edge-state spin texture in the fully polarized QSH regime. Arrows indicate the projection of the electron spin on a particular sublattice, with the two sublattices indicated by open and filled circles. The edge-state wavefunctions are evenly distributed on the two sublattices and have opposite spin polarizations, at least for an idealized armchair edge¹⁴.

by several orders of magnitude. This implies that the high-field $v = 0$ state has an incompressible bulk, consistent with the hypothesis of a ferromagnetic QSH state with conducting edge states and a bulk gap.

We probe the nature of the edge states through non-local transport measurements in which floating contacts are added along the sample edges²⁶. Unlike the chiral edge of a quantum Hall state, which carries current in only one direction, the QSH edge can carry current either way, with backscattering suppressed by the conservation of spin within the helical edge states. Because the carriers do not maintain their spin coherence within a metal contact, contacts equilibrate the counterpropagating states such that each length of QSH edge between contacts must be considered a single resistor of resistance h/e^2 . The two-terminal conductance results from the parallel addition of the two edges connecting the measurement probes:

$$G = \frac{e^2}{h} \left(\frac{1}{N_1+1} + \frac{1}{N_2+1} \right) \quad (1)$$

Here N_1 and N_2 are the respective numbers of floating contacts along each edge. Figure 2b shows the results of non-local two-terminal conductance measurements for the four distinct two-terminal measurement geometries available in a four-terminal device (Fig. 2a). Repeating the measurement for 18 cyclic permutations of the available contact configurations, we find that the results are well fitted by the simple model of equation (1) (Fig. 2c), despite large variations in the effective bulk aspect ratio. Notably, G_{exp} is always less than the value expected from the QSH model, suggesting some small but finite amount of backscattering or contact resistance. The combination of bulk incompressibility and non-local transport signatures of counterpropagating edge states leads us to conclude that the high-field metallic state observed indeed displays a QSH effect.

The QSH state realized here is equivalent to two copies of the quantum Hall effect, protected from mixing by the U(1) symmetry of spin rotations in the plane perpendicular to the magnetic field. As such, it constitutes

a topologically non-trivial state that is clearly distinct in its edge-state properties from the insulating state at fully perpendicular field. Capacitance measurements in the intermediate conductance regime reveal that the bulk gap does not close as the total field is increased (Fig. 3a). This rules out a conventional topological phase transition, in which case the bulk gap is required to close²⁷; the transition must thus occur by breaking the spin symmetry on which the QSH effect relies. In fact, a canted antiferromagnetic (CAF) state (Fig. 3b) that spontaneously breaks this symmetry is among the theoretically allowed $v = 0$ states^{11–13}. In this scenario, the canting angle is controlled by the ratio of the Zeeman energy, $g\mu_B B_\perp$ ($g = 2$, bare gyromagnetic ratio; μ_B , Bohr magneton), and the antiferromagnetic exchange coupling, which depends only on B_\perp . The observed conductance transition results from the edge gap closing (Fig. 3c) as the spins on the two graphene sublattices are slowly canted by the in-plane magnetic field, with the fully polarized QSH state emerging above a critical value of B_T (ref. 14). In the language of SPT insulators, the antiferromagnetic instability breaks the spin symmetry below this critical field, allowing the counterpropagating edge states to backscatter and acquire a gap²⁸.

Experimentally, the subcritical field regime is characterized by high-conductance peaks appearing symmetrically between $v = 0$ and $v = \pm 1$. We observe $G > e^2/h$ peaks in many samples with widely varying aspect ratios (Extended Data Fig. 5), which is inconsistent with diffusive bulk transport in a compressible Landau level²⁹. Measurements at different temperatures indicate that the peaks are metallic, even when the state at $v = 0$ is still strongly insulating (Fig. 4a). Moreover, the peaks exhibit the non-local transport behaviour of counterpropagating edge states (Fig. 4b); in particular, the peak conductance is always strictly less than e^2/h when the two edges are each interrupted by a floating contact. These results indicate that the conductance peaks are due to edge-state transport in the CAF state. The high conductance of these edge states, despite proximity to the strongly disordered etched graphene edge, implies that backscattering is at least partly suppressed. This is consistent with

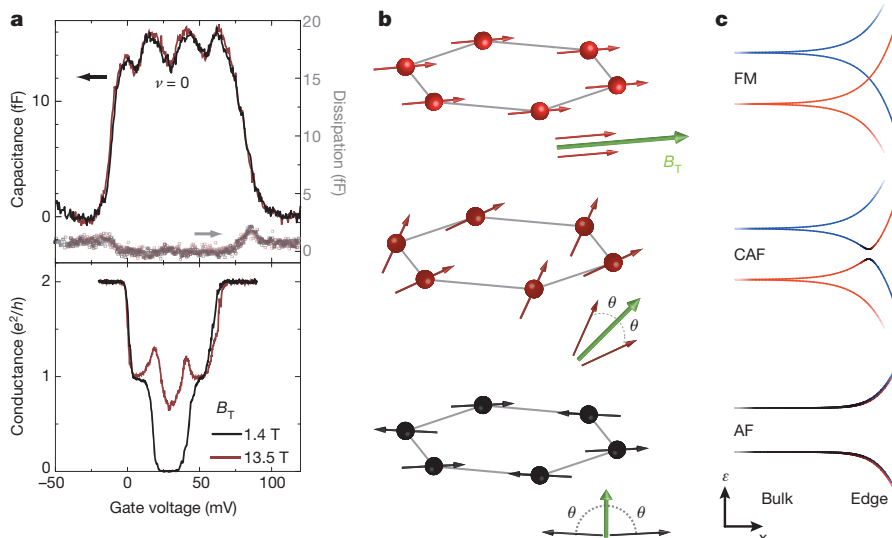


Figure 3 | Symmetry-driven quantum phase transition. **a**, Capacitance (top) and conductance (bottom) of device A at $B_\perp = 1.1$ T. The central dip in capacitance does not change with B_T at any point during the transition, implying that the bulk gap does not close. **b**, Bulk spin order in the three transition regimes. The balls and arrows are respectively schematic representations of the spin and sublattice textures of the ground-state wavefunctions and do not represent individual electrons; the electron density within the zLL at $v = 0$ is two electrons per cyclotron guiding centre. Insets, details of the relative alignment of the electron spins on the two sublattices. At large B_T , the bulk electron spins are aligned with the field (top panel), resulting in an emergent U(1) spin-rotation symmetry in the plane perpendicular to B_T . As the total magnetic field is reduced below some critical value (with B_\perp held constant), the spins on opposite sublattices cant with respect to each other while

maintaining a net polarization in the direction of B_T (middle panel). This state spontaneously breaks the U(1) symmetry, rendering local rotations of the electron spins energetically costly. For pure perpendicular fields (bottom panel), the valley isospin anisotropy energy overwhelms the Zeeman energy and the canting angle, θ , is close to 90° , defining a state with antiferromagnetic order. **c**, Low-energy band structure in the three phases¹⁴. ε is the energy and x is the in-plane coordinate perpendicular to the physical edge of the sample. The intermediate CAF phase smoothly interpolates between the gapless edge states of the QSH phase (top panel; FM, ferromagnetic) and the gapped edge of the perpendicular-field phase (bottom panel; AF, antiferromagnetic) without closing the bulk gap. Colour indicates the spin texture of the bands projected onto the magnetic field direction: red, aligned; blue, antialigned; black, zero net spin along the field direction.

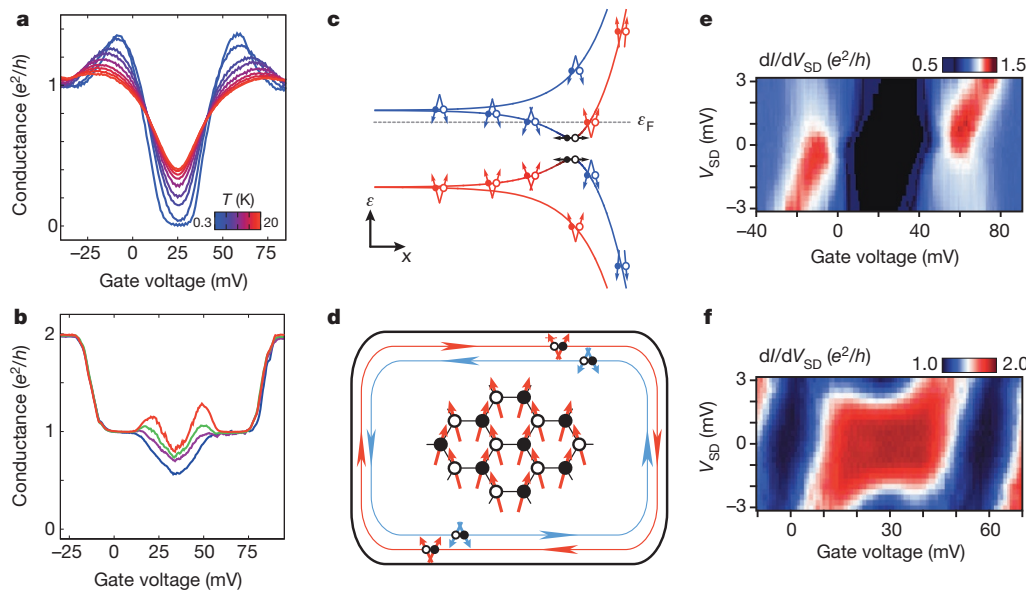


Figure 4 | Spin-textured edge states of the CAF phase. **a**, Temperature dependence in the intermediate-field regime for device C at $B_{\perp} = 5.9$ T and $B_T = 45.0$ T. The conductance peaks shows a metallic temperature coefficient, whereas the state at charge neutrality remains insulating. **b**, Non-local two-terminal conductance of device A at $B_{\perp} = 1.6$ T and $B_T = 26.1$ T. Colour-coding indicates contact geometry following the scheme in Fig. 2a. The height of the conductance peaks depends strongly on the configuration of floating contacts, indicating their origin in the gapped, counterpropagating edge states of the CAF phase. **c**, Schematic band diagram, including spin order, of the CAF edge states. For the electron and hole bands nearest to zero energy, the canting angle inverts near the sample edge, leading to counterpropagating edge states

with inverted CAF spin texture. The dashed grey line indicates the Fermi energy, ϵ_F , in the regime corresponding to one of the conductance peaks. **d**, Schematic of bulk order and edge-state spin texture in the CAF regime, following the convention of Fig. 2d. **e**, Differential conductance, dI/dV_{SD} , of device C in the CAF regime ($B_{\perp} = 5.9$ T, $B_T = 45.0$ T) in units of e^2/h . A constant source-drain voltage, V_{SD} , along with a 100- μ V, 313-Hz excitation voltage, are applied to one contact and the a.c. current is measured through the second, grounded contact. **f**, dI/dV_{SD} of device C in the QSH regime ($B_{\perp} = 2.7$ T, $B_T = 45.0$ T) in units of e^2/h . In both **e** and **f**, a symmetry is observed on reversing both V_{SD} and carrier polarity.

the theory of the band structure of the CAF state¹⁴ (Fig. 4c,d), in which the interpolation between the gapless QSH and gapped antiferromagnetic edge structures is achieved by means of a new kind of one-dimensional edge state in which counterpropagating modes have oppositely canted antiferromagnetic spin textures. Notably, existing theories of the CAF state are only rigorously applicable to the zero-carrier-density regime, in which case the CAF edge modes exist as excited states. The fact that we can access the CAF edge states by gating is somewhat surprising, because it implies that this spectrum is stable to small populations of the edge bands.

Questions remain about the precise nature of the QSH and CAF boundary modes. The measured G_{cnp} never reaches $2e^2/h$ even at the highest values of B_T , despite some of the devices showing a flat plateau around charge neutrality. Naively, backscattering within the QSH edge mode requires flipping an electron spin, for example by magnetic impurities, although such a process should be energetically unfavourable at high magnetic fields. More trivially, we cannot exclude that weakly conducting charge puddles connect the two edges (but not source and drain contacts), leading to backscattering across the bulk in the QSH regime. Spin-orbit effects may also play a part by spoiling the spin symmetry on which the helical edge states rely. Although the intrinsic spin-orbit coupling in graphene is thought to be weak¹⁷, the helical states may be uniquely sensitive to spin relaxation. Alternatively, the large Rashba-type spin-orbit coupling induced in the graphene under the gold contacts³⁰ may contribute a QSH-specific contact resistance that lowers the plateau conductance. The effects of disordered edges on helical edge transport have also not been addressed by modern theoretical treatments.

Nonlinear-transport measurements provide some additional insight into the nature of backscattering in the edge states. In both the QSH regime and the CAF regime, the nonlinear-transport data are invariant under simultaneous inversion of the carrier density and source-drain bias, V_{SD} (Fig. 4e,f). The data thus respect charge conjugation symmetry

within the graphene, possibly implying that the inelastic processes probed at large V_{SD} values are native to the electronic system. Notably, the nonlinear conductance is not invariant under reversal of source drain bias alone. We can understand this lack of symmetry as a natural consequence of dissipative edge transport in our system, where, in contrast to TRS topological insulators, the counterpropagating edge states can be spatially separated. Within this picture, reversing V_{SD} changes the current carried by the inner and outer counterpropagating edge states. If dissipation differs between the two states on a single edge and the two physical graphene edges are inequivalent, reversing V_{SD} can be expected to result in a different conductance.

The experiments presented in this Letter demonstrate the CAF-QSH crossover in monolayer graphene. In addition, they enable the study of QSH physics in a versatile material platform, enabling new experiments. Most importantly, the high-field graphene QSH system differs from the conventional TRS QSH state through the crucial role of interactions, which lead to the spontaneous breaking of spin symmetry that generates the gapped CAF edge states. We note that in this paper we have discussed experimental results in the context of mean-field treatments of interactions in the graphene zLL^{13,14}. Crucially, this treatment neglects the potential of the spin-ferromagnetic (or CAF) order parameter to reconstruct near the sample boundary^{10,12}, possibly leading to a qualitative change in the nature of the edge charge carriers. These results should inspire more careful experimental and theoretical work, both to understand the true nature of the edge states and to use them as a building block for realizing novel quantum circuits.

METHODS SUMMARY

Stacks of graphene, hexagonal boron nitride and graphite layers were fabricated by a dry transfer process. The sample surface was cleaned by high-temperature annealing in a reducing atmosphere after each transfer step and again after patterning of contacts by standard electron-beam lithography techniques. Before measurement, residual debris from the fabrication process was swept off the graphene flake with

an AFM tip operated in contact mode, the evidence of which is visible in the AFM micrograph inset in Fig. 2b.

Conductance measurements were made using a ~ 300 -Hz voltage bias, with root mean squared amplitude $V_{\text{rms}} = 100 \mu\text{V}$. The sample was immersed in ^3He liquid at 300 mK for all measurements except those shown in Fig. 4a, where the temperature is indicated, and those shown in Fig. 3, which were made at 150 mK with the sample immersed in a ^3He - ^4He mixture. The angle between the magnetic field and the graphene plane was controlled by a mechanical rotator. The alignment angle was determined using high-density Shubnikov-de Haas oscillations, ensuring reproducible alignment to better than 0.025° in the large-tilt-angle regime, $B_\perp \ll B_\parallel$. For multi-terminal devices (A and C), all measurements are done between two pairs of contacts (Fig. 3a, top configuration) unless otherwise indicated.

To measure capacitance, we used a cryogenic amplifier based on a high-electron-mobility transistor to construct a low-temperature capacitance bridge-on-a-chip, in which a 78-kHz a.c. excitation on the graphene sample was balanced against a variable phase and amplitude excitation on a known reference capacitor. The sample bias was 900 μV for the data set in Fig. 1b and 100 μV for that in Fig. 3a. The signal at the input of the cryogenic amplifier was first nulled by adjusting the reference excitation using a dual-channel a.c. signal generator, after which data were acquired off-balance by monitoring the in-phase and out-of-phase voltages at the balance point as a function of the applied d.c. sample bias. Biasing the transistor amplifier raised the base temperature of the cryostat, such that the temperature was 400 mK during acquisition of the data in Fig. 1b and 250 mK during acquisition of that in Fig. 3a.

Online Content Any additional Methods, Extended Data display items and Source Data are available in the online version of the paper; references unique to these sections appear only in the online paper.

Received 12 July; accepted 22 October 2013.

Published online 22 December 2013.

1. Ryu, S., Schnyder, A. P., Furusaki, A. & Ludwig, A. W. W. Topological insulators and superconductors: tenfold way and dimensional hierarchy. *N. J. Phys.* **12**, 065010 (2010).
2. Chen, X., Gu, Z.-C., Liu, Z.-X. & Wen, X.-G. Symmetry-protected topological orders in interacting bosonic systems. *Science* **338**, 1604–1606 (2012).
3. Hasan, M. Z. & Kane, C. L. Topological insulators. *Rev. Mod. Phys.* **82**, 3045–3067 (2010).
4. Qi, X.-L. & Zhang, S.-C. Topological insulators and superconductors. *Rev. Mod. Phys.* **83**, 1057–1110 (2011).
5. Chen, Y. L. *et al.* Massive Dirac fermion on the surface of a magnetically doped topological insulator. *Science* **329**, 659–662 (2010).
6. Xu, S.-Y. *et al.* Hedgehog spin texture and Berry's phase tuning in a magnetic topological insulator. *Nature Phys.* **8**, 616–622 (2012).
7. König, M. *et al.* Quantum spin Hall insulator state in HgTe quantum wells. *Science* **318**, 766–770 (2007).
8. Du, L., Knez, I., Sullivan, G. & Du, R.-R. Observation of quantum spin Hall states in InAs/GaSb bilayers under broken time-reversal symmetry. Preprint at <http://arxiv.org/abs/1306.1925> (2013).
9. Abanin, D. A., Lee, P. A. & Levitov, L. S. Spin-filtered edge states and quantum Hall effect in graphene. *Phys. Rev. Lett.* **96**, 176803 (2006).
10. Fertig, H. A. & Brey, L. Luttinger liquid at the edge of undoped graphene in a strong magnetic field. *Phys. Rev. Lett.* **97**, 116805 (2006).
11. Herbut, I. F. Theory of integer quantum Hall effect in graphene. *Phys. Rev. B* **75**, 165411 (2007).
12. Jung, J. & MacDonald, A. H. Theory of the magnetic-field-induced insulator in neutral graphene sheets. *Phys. Rev. B* **80**, 235417 (2009).

13. Kharitonov, M. Phase diagram for the $v = 0$ quantum Hall state in monolayer graphene. *Phys. Rev. B* **85**, 155439 (2012).
14. Kharitonov, M. Edge excitations of the canted antiferromagnetic phase of the $v = 0$ quantum Hall state in graphene: a simplified analysis. *Phys. Rev. B* **86**, 075450 (2012).
15. Hsieh, T. H. *et al.* Topological crystalline insulators in the SnTe material class. *Nature Commun.* **3**, 982 (2012).
16. Kindermann, M. Topological crystalline insulator phase in graphene multilayers. Preprint at <http://arxiv.org/abs/1309.1667> (2013).
17. Min, H. *et al.* Intrinsic and Rashba spin-orbit interactions in graphene sheets. *Phys. Rev. B* **74**, 165310 (2006).
18. Semenoff, G. W. Condensed-matter simulation of a three-dimensional anomaly. *Phys. Rev. Lett.* **53**, 2449–2452 (1984).
19. Checkelsky, J. G., Li, L. & Ong, N. P. Zero-energy state in graphene in a high magnetic field. *Phys. Rev. Lett.* **100**, 206801 (2008).
20. Yang, K., Das Sarma, S. & MacDonald, A. H. Collective modes and skyrmion excitations in graphene SU(4) quantum Hall ferromagnets. *Phys. Rev. B* **74**, 075423 (2006).
21. Alicea, J. & Fisher, M. P. A. Graphene integer quantum Hall effect in the ferromagnetic and paramagnetic regimes. *Phys. Rev. B* **74**, 075422 (2006).
22. Nomura, K., Ryu, S. & Lee, D.-H. Field-induced Kosterlitz-Thouless transition in the $N = 0$ Landau level of graphene. *Phys. Rev. Lett.* **103**, 216801 (2009).
23. Young, A. F. *et al.* Spin and valley quantum Hall ferromagnetism in graphene. *Nature Phys.* **8**, 550–556 (2012).
24. Maher, P. *et al.* Evidence for a spin phase transition at charge neutrality in bilayer graphene. *Nature Phys.* **9**, 154–158 (2013).
25. Mazo, V., Huang, C.-W., Shimshoni, E., Carr, S. T. & Fertig, H. A. Superfluid-insulator transition of quantum hall domain walls in bilayer graphene. Preprint at <http://arxiv.org/abs/1309.1563> (2013).
26. Roth, A. *et al.* Nonlocal transport in the quantum spin Hall state. *Science* **325**, 294–297 (2009).
27. Büttner, B. *et al.* Single valley Dirac fermions in zero-gap HgTe quantum wells. *Nature Phys.* **7**, 418–422 (2011).
28. Shitade, A. *et al.* Quantum spin Hall effect in a transition metal oxide Na_2IrO_3 . *Phys. Rev. Lett.* **102**, 256403 (2009).
29. Abanin, D. A. & Levitov, L. S. Conformal invariance and shape-dependent conductance of graphene samples. *Phys. Rev. B* **78**, 035416 (2008).
30. Marchenko, D. *et al.* Giant Rashba splitting in graphene due to hybridization with gold. *Nature Commun.* **3**, 1232 (2012).

Acknowledgements We acknowledge discussions with D. Abanin, A. Akhmerov, C. Beenakker, L. Brey, L. Fu, M. Kharitonov, L. Levitov, P. Lee and J. Sau. B.H. and R.C.A. were funded by the BES Program of the Office of Science of the US DOE, contract no. FG02-08ER46514, and the Gordon and Betty Moore Foundation, through grant GBMF2931. J.D.S.-Y. and P.J.-H. were primarily supported by the US DOE, BES Office, Division of Materials Sciences and Engineering, under award DE-SC0001819. Early fabrication feasibility studies were supported by NSF Career Award no. DMR-0845287 and the ONR GATE MURI. This work made use of the MRSEC Shared Experimental Facilities supported by the NSF under award no. DMR-0819762 and of Harvard's CNS, supported by the NSF under grant no. ECS-0335765. Some measurements were performed at the National High Magnetic Field Laboratory, which is supported by NSF Cooperative Agreement DMR-0654118, the State of Florida and the DOE. A.F.Y. acknowledges the support of the Pappalardo Fellowship in Physics.

Author Contributions A.F.Y. and J.D.S.-Y. had the idea for the experiment. J.D.S.-Y. and S.H.C. fabricated the samples. A.F.Y., J.D.S.-Y. and B.H. performed the experiments, analysed the data and wrote the paper. T.T. and K.W. grew the crystals of hexagonal boron nitride. R.C.A. and P.J.-H. advised on experiments, data analysis and writing the paper.

Author Information Reprints and permissions information is available at www.nature.com/reprints. The authors declare no competing financial interests. Readers are welcome to comment on the online version of the paper. Correspondence and requests for materials should be addressed to A.F.Y. (afy@mit.edu), J.D.S.-Y. (jdsy@mit.edu) or B.H. (benhunt@mit.edu).

METHODS

Sample fabrication. Samples consist of graphene/hexagonal boron nitride (hBN)/graphite stacks fabricated by a dry transfer process³¹. Samples are annealed in H₂-Ar atmosphere at 350 °C (ref. 32) after each transfer step and after patterning of contacts by standard electron-beam lithography techniques. Images of the final devices can be seen in Extended Data Fig. 1. Before measurement, residual debris from the fabrication process is swept off the graphene flake with an AFM tip operated in contact mode^{33,34} (the evidence of this is visible in the AFM micrograph inset in Fig. 2b). The methods used produce a random alignment angle between the graphene and hBN flakes. However, in the samples reported on in this paper, we do not see any evidence for moiré-induced band structure reconstructions³¹, suggesting that either the twist angle between the graphene and hBN lattices is large, or the coupling is weak (see Extended Data Fig. 8 for additional information).

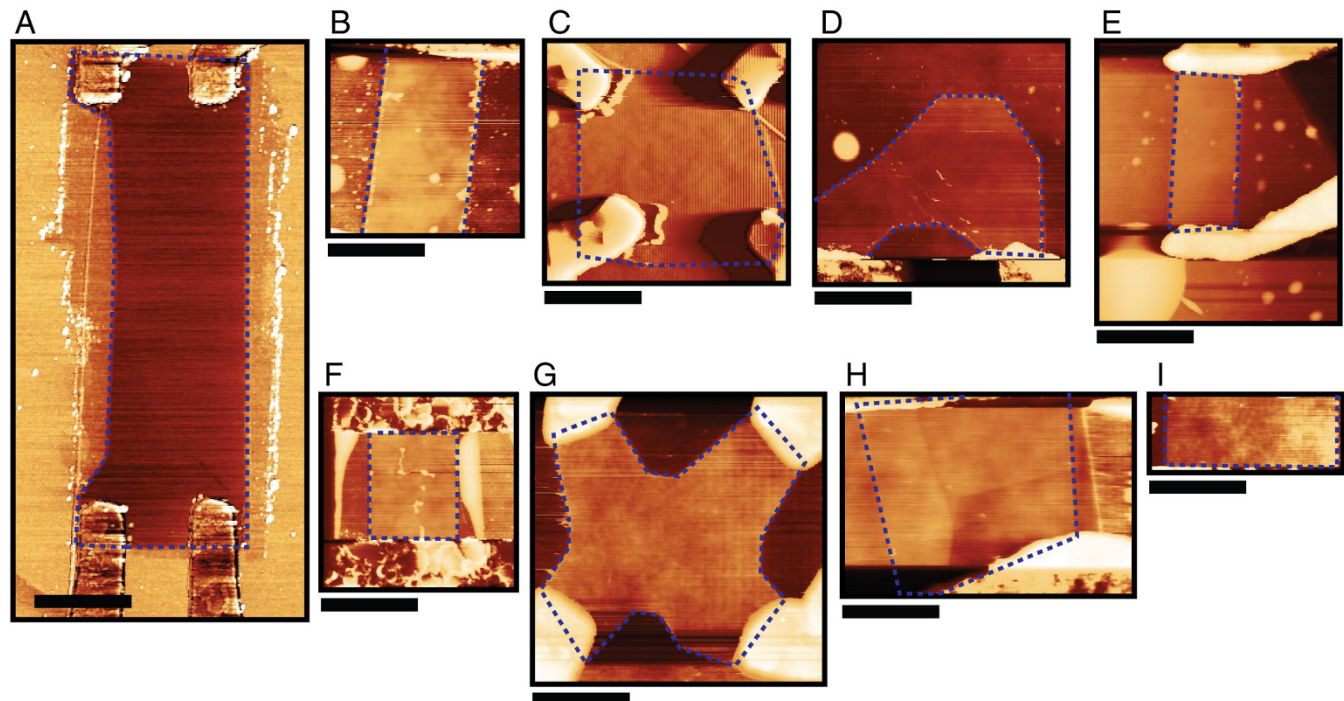
Conductance measurements. Conductance measurements were made using a ~300-Hz voltage bias, with $V_{ac} = 100 \mu\text{V}$. The sample was immersed in ³He liquid at 300 mK for all measurements except those shown in Fig. 4a, where the temperature is indicated, and those shown in Fig. 3, which were made at 150 mK with the sample immersed in a ³He–⁴He mixture. The angle between the magnetic field and the graphene plane was controlled by a mechanical rotator. The sample was aligned using high-density Shubnikov/de Haas oscillations, ensuring reproducible alignment to better than 0.025° in the large-tilt-angle regime, $B_{\perp} \ll B_T$. For multi-terminal devices (A and C), all measurements are done between two pairs of contacts (top configuration of Fig. 3a) unless otherwise indicated, ensuring that only two uninterrupted edges are being measured.

Capacitance measurements. To measure capacitance, we used a HEMT-based amplifier to construct a low-temperature capacitance bridge-on-a-chip³⁵. A schematic representation of the bridge geometry and electronics appears in Extended Data Fig. 7. In this geometry, an a.c. excitation on the graphene sample is balanced against a variable phase and amplitude excitation on a known reference capacitor, which is located near the sample. The sample bias was 900 μV for the data set in Fig. 1b and 100 μV for that in Fig. 3a, both of which were measured at 78 kHz. The signal at the input of the HEMT amplifier was first nulled by adjusting the reference

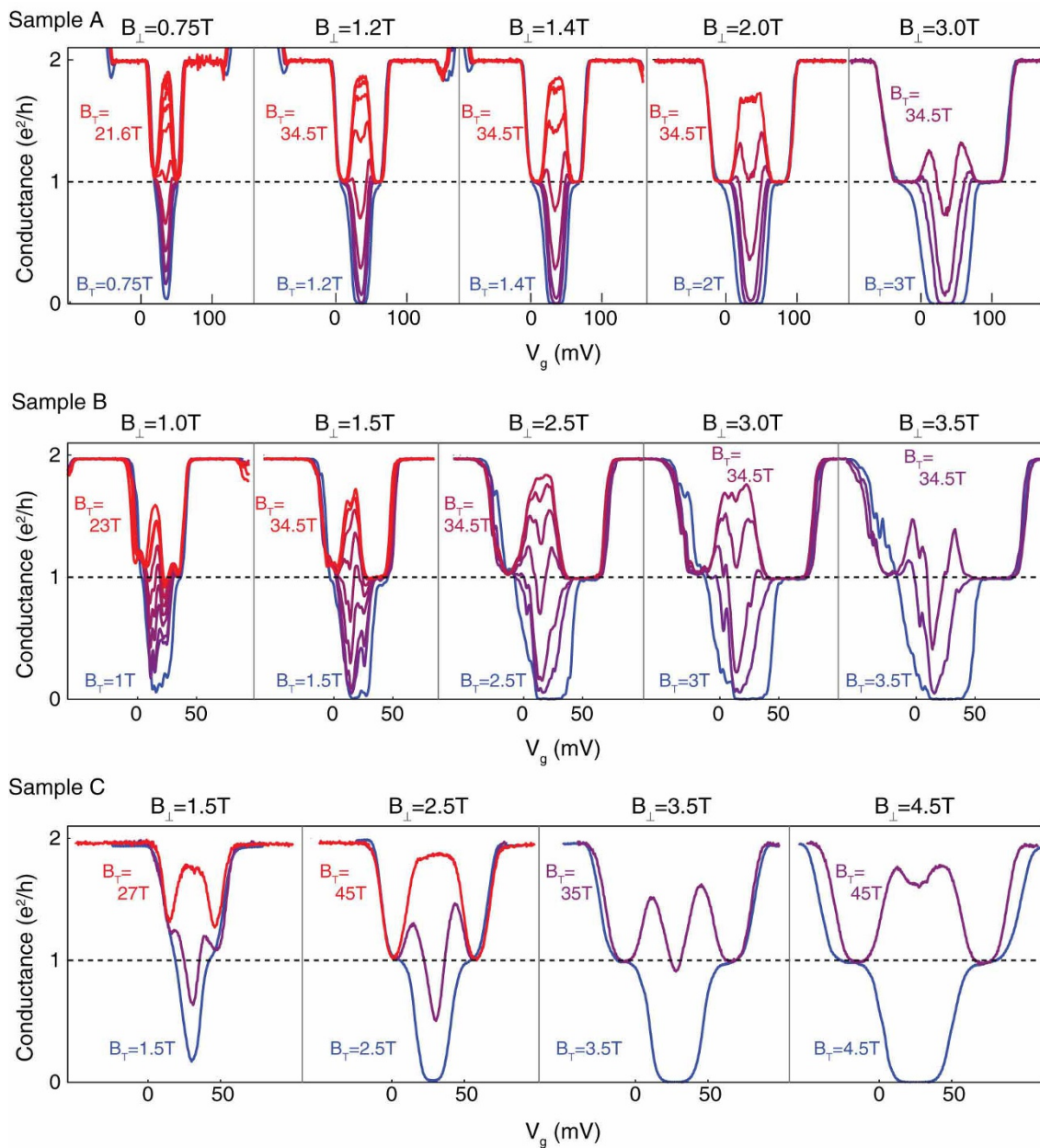
excitation using a homebuilt dual-channel a.c. signal generator, after which data were acquired off-balance by monitoring the in-phase and out-of-phase voltages at the balance point as a function of the applied d.c. sample bias. Biasing the transistor amplifier raised the base temperature of the cryostat, such that the temperature was 400 mK during acquisition of the data in Fig. 1b and 250 mK during acquisition of the data in Fig. 3a.

Extracting density-of-states information from capacitance measurements requires that the measurement frequency, f , be lower than the inverse charging time of the experimental system³⁶. Because incompressible regimes in quantum Hall samples are also highly resistive, contrast in the capacitance signal can be generated by the swing in sample resistance rather than density of states. In this case, capacitance minima appear because the sample can no longer charge on timescales of f^{-1} . Experimentally, such a transition is accompanied by a peak in the out-of-phase (dissipation) signal, which reaches a maximum when the sample resistance is $\sim 1/fC$, where C is the sample capacitance. In the capacitance data shown in Figs 1b and 3a, the dissipation signal is less than ~10% of the capacitive signal, suggesting that the observed features are mostly due to the density of states. We note that whether the capacitance dip associated with the metallic, high-field $v = 0$ state is due to incompressibility or high bulk resistance is immaterial to the conclusions in the paper: in either case, any metallic transport should be via edge states.

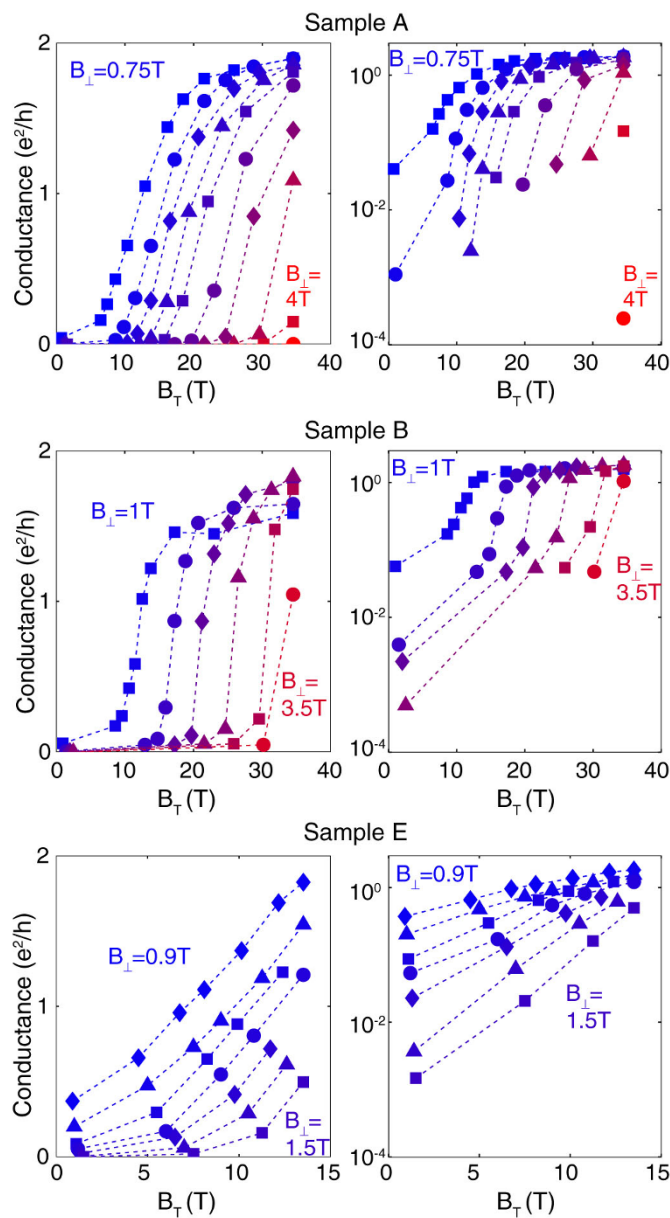
31. Hunt, B. et al. Massive Dirac fermions and Hofstadter butterfly in a van der Waals heterostructure. *Science* **340**, 1427–1430 (2013).
32. Dean, C. R. et al. Boron nitride substrates for high-quality graphene electronics. *Nature Nanotechnol.* **5**, 722–726 (2010).
33. Jalilian, R. et al. Scanning gate microscopy on graphene: charge inhomogeneity and extrinsic doping. *Nanotechnology* **22**, 295705 (2011).
34. Goossens, A. M. et al. Mechanical cleaning of graphene. *Appl. Phys. Lett.* **100**, 073110 (2012).
35. Ashoori, R. C. et al. Single-electron capacitance spectroscopy of discrete quantum levels. *Phys. Rev. Lett.* **68**, 3088–3091 (1992).
36. Goodall, R. K., Higgins, R. J. & Harrang, J. P. Capacitance measurements of a quantized two-dimensional electron gas in the regime of the quantum Hall effect. *Phys. Rev. B* **31**, 6597–6608 (1985).



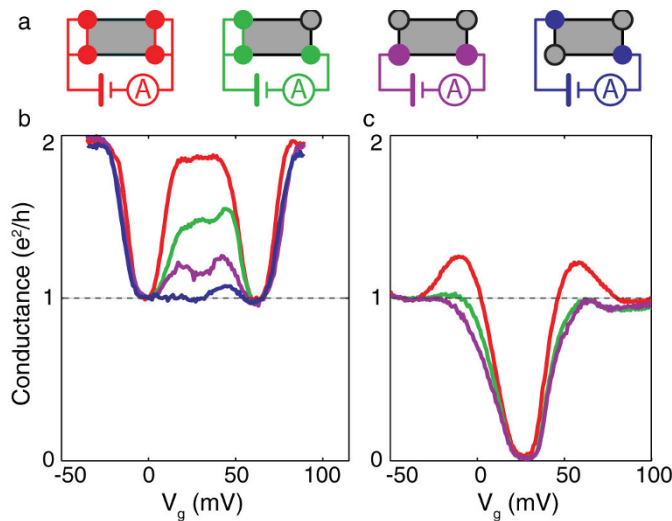
Extended Data Figure 1 | Images of measured devices. False-colour AFM images of the devices enumerated in Extended Data Table 1. Dashed lines outline the graphene boundary. Black scale bars correspond to 1 μm .



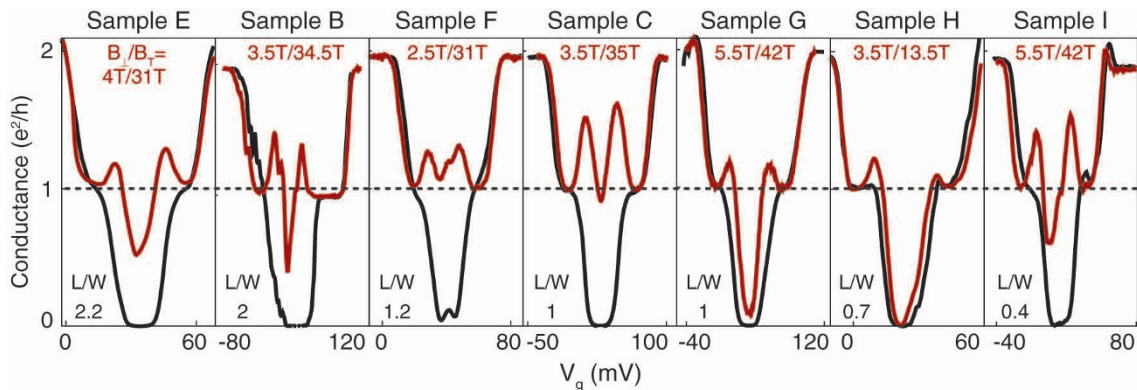
Extended Data Figure 2 | Conductance as a function of B_{\perp} , B_T and gate voltage for devices A, B and C. Colouring of lines from blue to red indicates increasing B_T , with B_{\perp} as indicated at the top of each panel.



Extended Data Figure 3 | G_{cnp} as a function of B_{\perp} and B_{T} for devices A, B and E. Correspondingly higher values of B_{T} are required to induce the transition for higher values of B_{\perp} . For device A, the curves correspond to $B_{\perp} = 0.75, 1, 1.2, 1.4, 1.6, 2, 2.5, 3, 3.5$ and 4T (blue to red). For device B, the curves correspond to $B_{\perp} = 1, 1.5, 2, 2.5, 3$ and 3.5T (blue to red). For device E, the curves correspond to $B_{\perp} = 0.9, 1, 1.1, 1.2, 1.3, 1.4$ and 1.5T (blue to red).

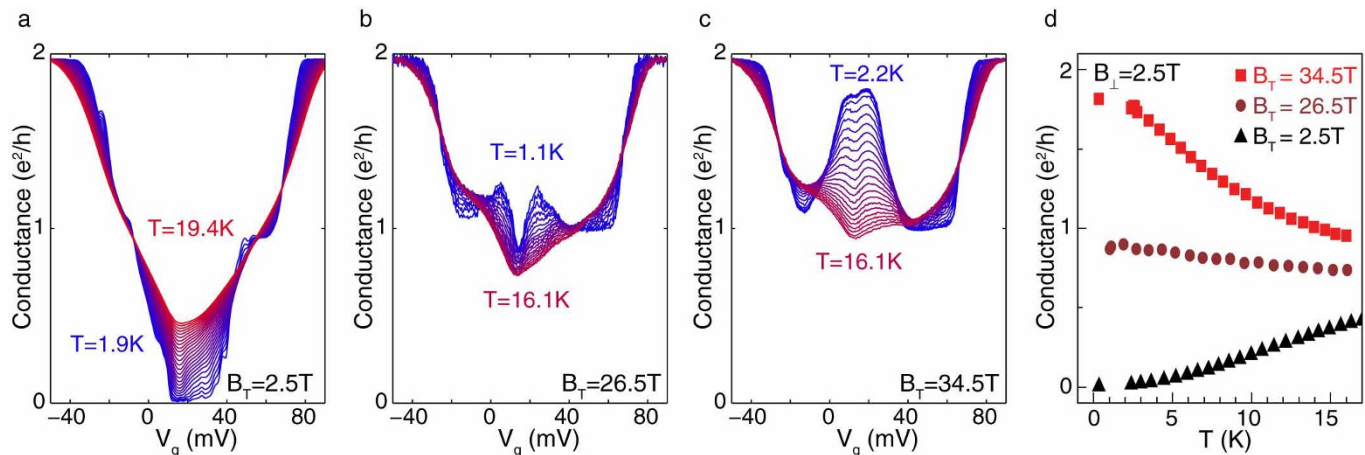


Extended Data Figure 4 | Nonlocal measurements for device C in the QSH and CAF regimes. In the main text, evidence for conduction via edge states in the QSH and CAF regimes is provided by non-local transport measurements in device A (Figs 2b and 4b). Owing to conduction through counterpropagating edge states, interrupting an edge with a floating contact decreases the two-terminal conductance much more than would be expected in a diffusive transport model. Here we provide an additional example of this behaviour for device C. **a**, Schematic of distinct two-terminal measurement topologies with different numbers of floating contacts (open circles). **b**, QSH regime, $B_{\perp} = 2.7$ T and $B_T = 45$ T. **c**, CAF regime, $B_{\perp} = 5.9$ T and $B_T = 45$ T. Curves are colour-coded according to the measurement schematics, as in the main text. Owing to a small gate leak in one of the contacts, these specific non-local measurements underestimate the conductance by a scale factor that was adjusted for by fitting the $v = -1$ plateau to a conductance of e^2/h .



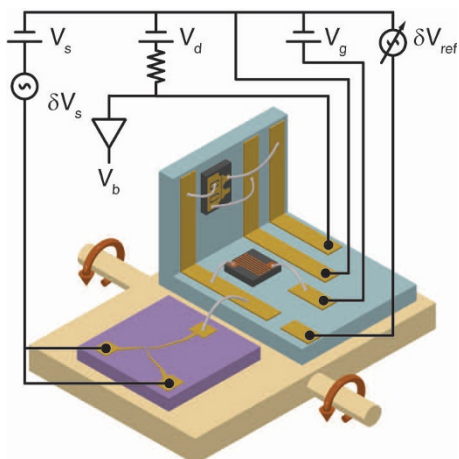
Extended Data Figure 5 | Double conductance peaks in seven different devices. A generic feature of the intermediate regime between the insulating and metallic QSH regimes is the appearance of double conductance peaks close to $v = 0$. The figure shows two-terminal conductance versus back-gate voltage, V_G . Purely perpendicular magnetic field only ($B_T = B_{\perp}$, black lines) results in

an insulating state at $v = 0$. Increasing the total magnetic field while keeping the perpendicular component constant ($B_T > B_{\perp}$, red lines), induces a transition to the CAF with an associated double conductance peak feature. Devices are ordered from left to right by descending aspect ratio.

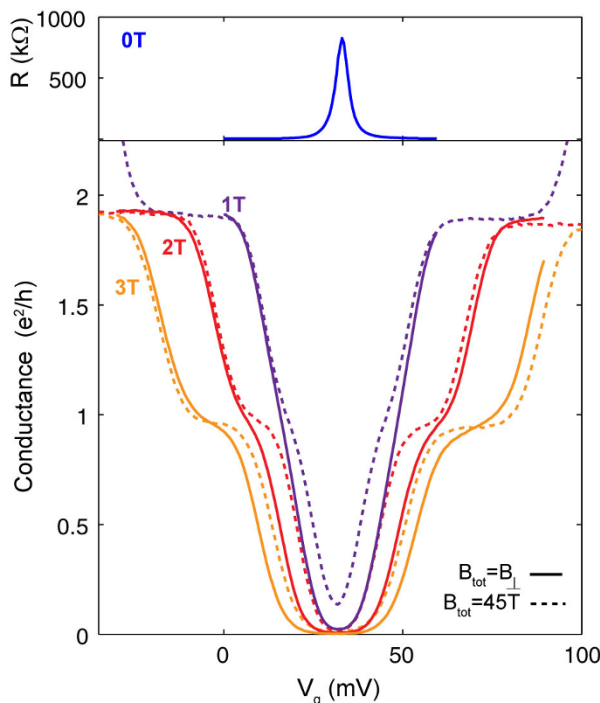


Extended Data Figure 6 | Temperature dependence of the charge-neutrality point conductivity for device B. **a–c,** Gate sweeps for device B at constant $B_{\perp} = 2.5$ T and $B_T = 2.5$ (a), 26.5 (b) and 34.5 T (c). **d,** Conductance at the charge-neutrality point as a function of temperature for the data in a–c. A clear insulating dependence ($\partial G/\partial T > 0$) is observed for $B_{\perp} = B_T$. With increased

B_T , in the intermediate regime, the double conductance peaks between $v = 0$ and $v = \pm 1$ have a weakly metallic temperature dependence ($\partial G/\partial T < 0$) whereas G_{cnp} is very weakly insulating. In the QSH regime ($B_T \gg B_{\perp}$), where the conduction is along edge channels, the temperature dependence at $v = 0$ is metallic.



Extended Data Figure 7 | Schematic diagram of the capacitance bridge-on-a-chip in a tilted magnetic field. The magnetic field points up in the diagram. Beige: sample stage, showing axis of rotation (red arrows). Purple: graphene sample mount. Blue: transistor mount with 90° bend. The HEMT is mounted on the face angled at 90° to the graphene sample mount and with the plane of its 2D conduction channel perpendicular to the sample-stage axis of rotation. A single wire bond connects the two mounts, from the graphite back gate to the balance point of the capacitance bridge. The transistor is gated by applying V_G to the balance point/graphite back gate through a 100-MΩ chip resistor. Combined with the total capacitance of the balance point to ground ($\sim 3\text{ pF}$), this sets the low-frequency cut-off for the measurement at $\sim 1\text{ kHz}$. The density of electrons in the graphene sample is determined by the d.c. voltage difference between the graphene sample and the graphite back gate, namely by $V_s - V_G$. In the main text, this is compensated for and all capacitance measurements are shown as functions of the graphite gate voltage relative to grounded graphene. All components shown in black are at room temperature.



Extended Data Figure 8 | Tilted-field magnetotransport in zero-field insulating monolayer graphene. In a fraction of devices with the same geometry as those discussed in the main text, we find that, rather than a conductivity of $\sim e^2/h$ at charge neutrality, these devices instead have insulating behaviour at the charge-neutrality point at zero applied magnetic field. We ascribe this insulating behaviour to the opening of a bandgap at the charge-neutrality point owing to the effect of an aligned hBN substrate³¹. The top panel shows the resistance of the device in zero magnetic field. This device has a resistance of 825 kΩ at the charge-neutrality point in zero magnetic field and at $T = 0.3$ K. As with the devices described in the main text, the insulating state becomes stronger in a perpendicular magnetic field. In the bottom panel, solid lines are gate sweeps at constant $B_\perp = 1, 2$ and 3 T and $B_T = B_\perp$. Dashed lines are for the corresponding sequence with $B_\perp = 1, 2$ and 3 T but $B_T = 45$ T. Data taken at 0.3 K. Semiconducting graphene samples do not show any sign of QSH-type physics, at least up to 45 T. Even for $B_\perp = 1$ T and $B_T = 45$ T, the conductance at the charge-neutrality point increases only slightly, from $0.02e^2/h$ with zero in-plane field to $0.14e^2/h$ with $B_T = 45$ T. This is understandable, because, even neglecting interaction effects, closing a moiré-induced band gap of $\Delta = 10$ meV requires a Zeeman field of nearly $\Delta/g\mu_B \approx 85$ T. We note that in these samples, the ground state at $B_T = B_\perp$ may not be an antiferromagnet.

Extended Data Table 1 | Physical parameters of measured devices

Sample Name	BN Thickness (nm)	Sample Dimensions LxW (μm)	Aspect Ratio (L/W)
A	14	3.6 x 1.4	2.6
B	9	1.8 x 0.9	2
C	8.4	1.2 x 1.2	1
D	4.2	2.1 x 0.7	3
E	3.4	1.6 x 0.7	2.2
F	4	1.1 x 0.9	1.2
G	4.4	1 x 1	1
H	2.2	1.4 x 2	0.7
I	3.8	0.7 x 1.8	0.4

The studied devices consist of sequentially stacked flakes of thin graphite, hBN and monolayer graphene on an insulating Si wafer with 285 nm of thermally grown SiO_2 . The bottom graphite layer serves as a local gate electrode as well as to screen charge inhomogeneity in the graphene. The table lists the details of the samples discussed in the main text (devices A–C), as well as those of the additional samples discussed in Methods and Extended Data (devices D–I).